

Cine and late gadolinium enhancement MRI registration and automated myocardial infarct heterogeneity quantification

Fumin Guo^{1,2}  | Philippa R. P. Krahn^{1,2}  | Terenz Escartin^{1,2} | Idan Roifman³ | Graham Wright^{1,2}

¹Sunnybrook Research Institute, University of Toronto, Toronto, Canada

²Department of Medical Biophysics, University of Toronto, Toronto, Canada

³Sunnybrook Health Sciences Center, University of Toronto, Toronto, Canada

Correspondence

Fumin Guo, Department of Medical Biophysics, University of Toronto, 2075 Bayview Avenue, Toronto M4N 3M5, Canada.
Email: fumin.guo@utoronto.ca

Funding information

This work was funded by Canadian Institutes of Health Research (CIHR) MOP: #93531; Ontario Research Fund; and GE Healthcare. Fumin Guo is supported by a Banting postdoctoral fellowship

Purpose: To develop an approach for automated quantification of myocardial infarct heterogeneity in late gadolinium enhancement (LGE) cardiac MRI.

Methods: We acquired 2D short-axis cine and 3D LGE in 10 pigs with myocardial infarct. The 2D cine myocardium was segmented and registered to the LGE images. LGE image signal intensities within the warped cine myocardium masks were analyzed to determine the thresholds of infarct core (IC) and gray zone (GZ) for the standard-deviation (SD) and full-width-at-halfmaximum (FWHM) methods. The initial IC, GZ, and IC + GZ segmentations were postprocessed using a normalized cut approach. Cine segmentation and cine-LGE registration accuracies were evaluated using dice similarity coefficient and average symmetric surface distance. Automated IC, GZ, and IC + GZ volumes were compared with manual results using Pearson correlation coefficient (r), Bland-Altman analyses, and intraclass correlation coefficient.

Results: For $n = 87$ slices containing scar, we achieved cine segmentation dice similarity coefficient = 0.87 ± 0.12 , average symmetric surface distance = 0.94 ± 0.74 mm (epicardium), and 1.03 ± 0.82 mm (endocardium) in the scar region. For cine-LGE registration, dice similarity coefficient was 0.90 ± 0.06 and average symmetric surface distance was 0.72 ± 0.39 mm (epicardium) and 0.86 ± 0.53 mm (endocardium) in the scar region. For both SD and FWHM methods, automated IC, GZ, and IC + GZ volumes were strongly ($r > 0.70$) correlated with manual measurements, and the correlations were not significantly different from interobserver correlations ($P > .05$). The agreement between automated and manual scar volumes (intraclass correlation coefficient = 0.85-0.96) was similar to that between two observers (intraclass correlation coefficient = 0.81-0.99); automated scar segmentation errors were not significantly different from interobserver segmentation differences ($P > .05$).

Conclusions: Our approach provides fully automated cine-LGE MRI registration and LGE myocardial infarct heterogeneity quantification in preclinical studies.

KEYWORDS

cine MRI, LGE, myocardial infarct quantification, registration, segmentation

1 | INTRODUCTION

Myocardial infarction (MI) due to prolonged ischemia in the heart leads to the development of myocardial scarring, a hallmark feature of coronary artery disease. Scar-related ventricular tachycardia is a particularly dangerous cardiac arrhythmia and represents a leading cause of sudden cardiac death (SCD).^{1,2} Implantable cardioverter defibrillator (ICD) therapy can effectively terminate ~90% of life-threatening ventricular tachycardia episodes³ and reduce overall mortality by ~40% in 1 year.⁴ Current guidelines for identifying candidates for ICD therapies to prevent SCD rely on left ventricle ejection fraction <35% as the primary criterion.⁵ However, this measure fails to identify one-third of SCD cases,⁶ and in patients who are identified based on this criterion, the average annual rate of appropriate ICD firing is only ~5%.⁷ Accordingly, there is an urgent need for better risk stratification to select candidates who would benefit the most from ICD therapies.

Post-MI, the damaged heart muscle undergoes structural and functional remodeling that creates heterogeneous fibrosis in the infarcted area,^{8,9} which can form the arrhythmogenic substrates that are responsible for ventricular tachycardia and SCD events.^{9,10} Late gadolinium enhancement (LGE) MRI has been established as the clinical standard for evaluating myocardial tissue composition, including MI.¹¹ Using LGE MRI, MI can be characterized as regions of dense fibrosis (infarct core [IC]) and regions with a mixture of viable myocytes and collagen strands (gray zone [GZ]).^{12,13} Numerous investigations have demonstrated the prognostic value of LGE-derived biomarkers for cardiac structural and functional abnormality phenotyping and SCD risk stratification. In particular, the extent of GZ, independent of other clinical- and MRI-derived variables, is strongly associated with ventricular tachycardia inducibility, ICD events, and cardiac mortality.^{12,14-16}

Quantification of MI heterogeneity (ie, IC, GZ, and healthy myocardium) is crucial for integrating LGE MRI for SCD risk stratification and efficacious patient selection for ICD therapies. Accordingly, a number of algorithms have been developed for MI heterogeneity quantification in LGE images, including standard-deviation (SD); full-width-at-half-maximum (FWHM); clustering; model fitting; graph cut/continuous max-flow; and recently, deep learning methods for direct scar quantification, as previously summarized.^{17,18} SD and FWHM-based methods remain the most widely used^{15,19,20} because of the clinically significant predictors of mortality they provide. Although effective and straightforward to implement, SD and FWHM-based methods are limited by a number of factors that hamper efficient clinical workflow. Current implementations mainly use LGE images and require: 1) manual segmentation of endocardial and epicardial contours to obtain the myocardial volume, and

2) manual delineation of a remote myocardial region as the reference for the SD and FWHM methods and of a hyperenhanced region for the FWHM method. In addition, substantial manual corrections are often required to identify regions of microvascular obstruction within scar and to remove blood pool and pericardial partial volume artifacts. These tedious and time-consuming user interactions introduce substantial user variability and are not compatible with efficient clinical workflow. These issues become more prominent because high-resolution 3D LGE is increasingly used in characterizing MI in recognition of the fact that scar quantification is dependent on image resolution.^{21,22} Furthermore, the population of potential individuals with prior infarct is growing due to improved preventative patient care and survival after acute MI,² which increases clinical workload and necessitates high-throughput workflows.

MRI protocols using cine acquisitions provide high-resolution, multidimensional visualization of cardiac structural and functional abnormalities with excellent soft tissue contrast.²³ Here, we proposed to employ the myocardial structural information provided by cine MRI to facilitate LGE MI heterogeneity quantification. In particular, our objective was to develop a way to fully automate the existing SD and FWHM methods for rapid and reproducible MI heterogeneity quantification. This work represents an important step toward clinical studies of fully automated analysis of LGE MRI.

2 | METHODS

2.1 | Animal preparation

We evaluated 10 Yorkshire swine (20-25 kg, University of Guelph, Guelph, Canada) in accordance with the study protocols approved by The Animal Care Committee of Sunnybrook Health Sciences Centre. Animals were sedated through intramuscular injection of ketamine (30 mg/kg) and atropine (0.05 mg/kg) and were maintained at a surgical stage of anesthesia by continuously delivering isoflurane gas (1%-5%) via mechanical ventilation (20-25 breaths/min). A bolus of amiodarone (50 mg/mL) and lidocaine (30 mL of 2% lidocaine in 250 mL of saline, as needed) was administered to mitigate arrhythmia, as previously described.^{13,24} Following catheterization, the left anterior descending artery was occluded distal to second diagonal branch using an inflated balloon dilation catheter (Sprinter Legend Balloon Catheter, Medtronic, Minneapolis, MN) for ~90 min. Blood flow was restored and then confirmed using X-ray fluoroscopy (OEC 9800, GE Healthcare, Milwaukee, WI) within 5 min of balloon deflation and retraction.²⁵ The animals were recovered from anesthesia and allowed to heal for 5-6 weeks to create heterogeneous infarct.

2.2 | Image acquisition

MR imaging was performed on a 3 Tesla scanner (MR 750, General Electric Healthcare, Milwaukee, WI) with a 16-channel anterior cardiac coil array, as previously described.²⁴ For cine MRI, 2D short-axis slices covering the ventricular chambers were acquired using a respiratory-gated balanced SSFP sequence (repetition time/echo time/flip angle = 4.0 ms/1.8 ms/45°, field-of-view = 24-30 × 24-30 cm², matrix size = 256 × 256, slice thickness = 5-6 mm, number of slices = 13-20, number of phases = 20, views per segment = 8, number of excitations = 1, bandwidth = 125 KHz). 3D LGE was performed ~10-15 min following injection of gadolinium-DPTA (0.2 mmol/kg, Magnevist, Berlex Inc., Wayne, NJ) using an inversion recovery fast gradient echo sequence with respiratory navigation (repetition time/echo time/flip angle = 3.7 ms/1.6 ms/15°, field-of-view = 24-30 × 24-30 × 6-10 cm³, matrix size = 256 × 256 × 40-140, bandwidth = 31.25 KHz).

2.3 | Image analysis and MI heterogeneity quantification

Figure 1 provides a schematic of the fully automated algorithm workflow that integrated cine myocardial segmentation, cine-LGE registration, and LGE scar quantification.

Cine myocardium segmentation was performed using a widely used U-net²⁶ that was trained on 20 stacks of 2D cine images from a separate group of 10 pigs scanned using the same MR system with the same MR protocols (this dataset was not used for algorithm performance evaluation). The myocardium was segmented in each of the 20 stacks of cine images using CVI-42 v4.1.8 software (Circle Cardiovascular

Imaging, Calgary, Alberta, Canada) to train the U-net in 2D: number of levels = 5, number of features in the first level = 16, number of epochs = 200, number of updates per epoch = 100, batch size = 15, optimizer = Adam, learning rate = 0.0001, loss function = cross entropy. Data augmentation, including random rotation (-60~60 degrees), translation (-30~30 pixels), resizing (0.8~1.2 times), and intensity scaling (0.8~1.2 times), as well as Monte Carlo dropout (dropout rate = 0.5) during training and testing, were performed to improve the robustness and minimize overfitting of U-net training. The automated myocardial infarct quantification algorithm was implemented in 3 steps as follows:

Step 1: The target cine images (slice thickness = 5-6 mm) at approximately end diastole were interpolated in the through-plane direction to approximately isotropic voxel sizes. The trained U-net model was applied to the interpolated cine data to generate 50 Monte Carlo dropout predictions for each interpolated cine volume, which were combined to obtain a single segmentation using a simultaneous truth and performance level estimation algorithm.²⁷

Step 2: The interpolated cine images were registered to the 3D LGE data using an affine registration algorithm that employed block matching.²⁸ The affine registration results were refined using a deformable registration step that utilized a modality independent neighbor descriptor for cine-LGE image similarity measurements and B-spline free-form deformation for regularization.²⁹ The resulting deformation field was used to warp the cine myocardium masks provided by the U-net (step 1) into the 3D LGE space.

Step 3: The warped cine myocardium masks were used to restrict the LGE MI heterogeneity analysis, which was implemented in 3 substeps as follows:

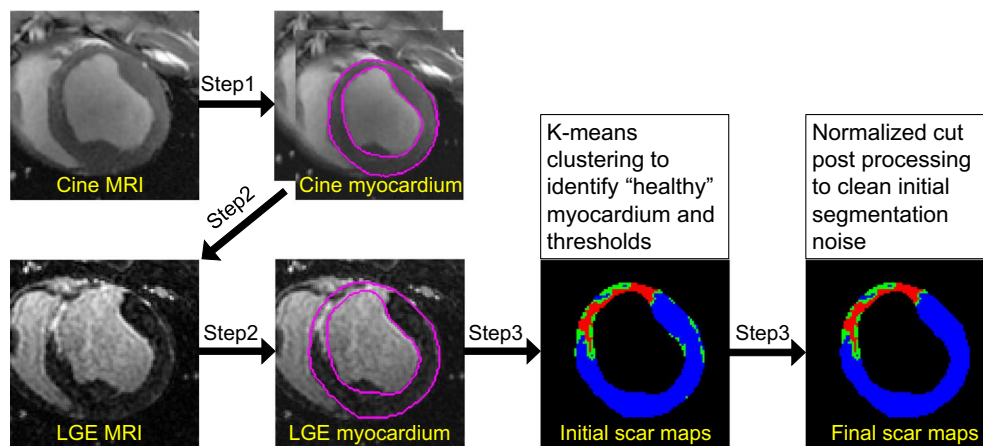


FIGURE 1 Schematic for our automated algorithm pipeline. 2D cine stacks and 3D LGE MR images were inputs to the pipeline. Step 1: The original 2D cine images were interpolated to approximately isotropic voxel sizes, and the myocardium was segmented using a U-net. Step 2: The interpolated cine was registered to the 3D LGE, and the resulting deformation field was used to warp the cine myocardium masks derived in step 1. Step 3: The warped cine myocardium masks were used to characterize MI heterogeneity based on the SD and FWHM methods. LGE, late gadolinium enhancement; MI, myocardial infarction

Step 3a: LGE image signal intensities within the warped cine myocardium masks were clustered into 3 classes using a k-means clustering approach. The cluster with the lowest signal intensities was used as the initial remote region.

Step 3b: The initial remote region in step 3a was postprocessed by keeping the largest connected component, which was used as the remote region for the SD and FWHM methods. For the SD-based method, the mean ($mean_{rmt}$) and SD (std_{rmt}) of the signal intensities in the refined remote region were used to determine the thresholds (T) of GZ and IC,¹⁵ that is, $T_{GZ}^{SD} = mean_{rmt} + 2 * std_{rmt}$ and $T_{IC}^{SD} = mean_{rmt} + 5 * std_{rmt}$. For the FWHM method, the maximal signal intensities in the refined remote region and the warped cine myocardial mask were used to determine the thresholds (T) of GZ and IC,¹² that is, $T_{GZ}^{FWHM} = max_{rmt}$ and $T_{IC}^{FWHM} = 0.5 * max_{myo}$, where max_{rmt} and max_{myo} represent the maximal signal intensities in the refined remote region and the entire myocardium, respectively. The 2 thresholds were used to identify the initial IC, GZ, and healthy myocardium regions for each quantification method. This step was used to eliminate the need for manual selection of a remote region for the SD and FWHM methods.

Step 3c: The initial IC, GZ, and healthy myocardium regions were postprocessed using a normalized cut approach³⁰ to correct the segmentation errors. In particular, the initial IC and GZ clusters were merged as a single region whereby the largest connected component and the remainder were temporarily labeled as “1” and “0,” respectively. The X - Y coordinates of the pixels in the merged region were used to generate image features in the form of $f(x) = \{X(x), Y(x)\}$, where $X(x)$ and $Y(x)$ represent the X - Y coordinates of pixel x . The normalized cut approach was formulated as: $NC(S) = -\frac{S^T AS}{1AS}$, where A is a matrix that encodes the similarity between image features $f(x)$ at any 2 pixels, and S represents the segmentation. The normalized cut model was efficiently solved through upper-bound linearization.^{31,32} Upon algorithm convergence and within the merged IC and GZ region, the pixels labeled “0” were combined with the initial healthy myocardium in step 3b, and the pixels labeled “1” were assigned the original IC and GZ labels in step 3b. This step was used to effectively reduce manual corrections of initial suboptimal MI quantification results provided by both the manual and automated algorithms.

2.4 | Algorithm validation

Algorithm performance was evaluated for cine myocardium segmentation, cine-LGE registration, and automated LGE MI heterogeneity quantification. In particular, cine myocardium segmentation and cine-LGE registration were evaluated both globally for the entire myocardium and

regionally for the region containing scar, as illustrated in Supporting Information Figure S1. Cine myocardium segmentation accuracies were determined using dice similarity coefficient (DSC) and average symmetric surface-distance (ASSD)³² between the U-net and manual cine myocardium masks. Cine-LGE registration accuracy was quantified by comparing the warped cine manual masks and the LGE myocardium manual segmentation using DSC and ASSD to only evaluate the effects of the registrations, as previously suggested.^{33,34} Note that cine and LGE myocardium manual segmentations were used for cine-LGE registration accuracy evaluation, whereas cine myocardium U-net segmentation was used for LGE MI heterogeneous analysis in section 2.3 steps 2-3. Cine and LGE myocardium manual segmentation were performed by a single observer (F.G., with 2.5 years' experience in cardiac MRI manual segmentation) at least 2 months apart; and the manual masks were independently reviewed, corrected, and approved by 2 experts each with more than 10 years' experience in cardiac MRI segmentation. LGE myocardium manual segmentation was performed twice separated by 1 month, and the 2 sets of manual segmentation were merged using a simultaneous truth and performance level estimation algorithm for cine-LGE registration accuracy evaluation.

To characterize intra- and interobserver manual segmentation performance, 2 observers (F.G. and T.E.) manually selected a remote region within the LGE following the previous guidelines^{12,19} 3 times on 3 different days. The 2 LGE myocardium manual segmentations and the 3 manual remote regions were used to generate 6 sets of manual LGE MI heterogeneity results using the SD and FWHM methods for each observer (F.G. and T.E.). The 12 sets of manual IC, GZ, and IC + GZ volumes were averaged and compared with automated algorithm measurements for the SD and FWHM methods. Similarly, the IC, GZ, and IC + GZ volumes in the 6 sets of manual results were averaged for each observer (F.G. and T.E.), and the 2 observers' measurements were compared. The absolute differences of automated versus manual ($Diff_{Aut-Man}$) and F.G. versus T.E.'s manual ($Diff_{Man-Man}$) segmentation volumes were calculated for each slice. Both the initial manual and initial automated results were “noisy” and were postprocessed using the normalized cut algorithm in step 3 in section 2.3.

2.5 | Statistical analysis

Pearson correlation coefficients (r), Bland-Altman analyses, and paired t tests were used to determine the relationships of IC, GZ, and IC + GZ volumes provided by the automated and manual methods. Correlation coefficients (r) were compared using Fisher r -to- z transformations.³⁵ The intraclass correlation coefficient (ICC) was used to measure the absolute agreement between automated and manual scar volumes

as well as multi-observer repeated manual segmentation. In addition, $\text{Diff}_{\text{Aut-Man}}$ and $\text{Diff}_{\text{Man-Man}}$ were compared for IC, GZ, and IC + GZ using paired t tests. Normality of data distribution was determined using Shapiro-Wilk tests, and when significant, nonparametric tests were performed. The statistical analyses were performed using Statistical Package for the Social Science (SPSS) version 23 (SPSS Inc., Chicago, IL). Results were considered significant when the probability of making a type I error was less than 5% ($P < .05$).

3 | RESULTS

Figure 2 shows representative results of cine myocardium segmentation using a U-net and cine-LGE registration using an affine and a deformable registration method.

Table 1 provides the cine myocardium segmentation and cine-LGE registration accuracies for $n = 87$ slices containing scar from 10 pigs. For segmentation of the entire myocardium, we achieved mean DSC of 0.879 ± 0.097 , ASSD of 0.91 ± 0.51 mm for the epicardium, and 0.93 ± 0.56 mm for the endocardium. When restricting the analysis to the scar

region, we obtained a slightly lower DSC of 0.865 ± 0.119 and higher ASSD of 1.03 ± 0.82 mm for the epicardium, with very similar ASSD of 0.94 ± 0.74 mm for the endocardium. For cine-LGE registration, we observed a mean DSC of 0.913 ± 0.050 , ASSD of 0.71 ± 0.33 mm for the epicardium, and 0.79 ± 0.41 mm for the endocardium by comparing cine and LGE myocardium manual segmentation. Similarly, we observed a slightly lower DSC of 0.901 ± 0.064 and higher ASSD of 0.86 ± 0.53 mm for the endocardium, whereas the ASSD of the epicardium was very similar when comparing the analysis restricted to the scar region versus for the entire myocardium. In addition, we compared cine U-net myocardium segmentation and LGE manual myocardium segmentation after cine-LGE registration (automated LGE MI analysis in Table 1). For the entire endocardium, we observed DSC of 0.859 ± 0.105 and ASSD of 1.04 ± 0.54 mm for the epicardium and 1.09 ± 0.55 mm for the endocardium; for the scar region, DSC was 0.832 ± 0.124 , and ASSD was 1.16 ± 0.82 mm for the epicardium and 1.28 ± 0.78 mm for the endocardium.

Figure 3 provides examples of LGE MI heterogeneity quantification results generated using the automated algorithm and the manual segmentation based on the SD method. For

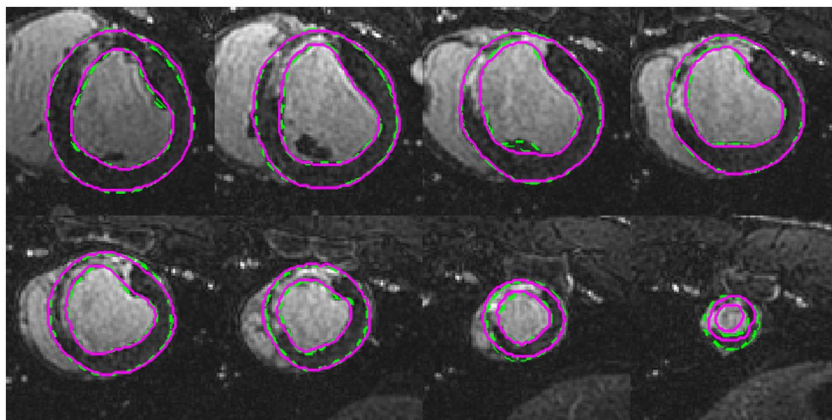


FIGURE 2 Representative myocardium segmentation delineated and overlaid on LGE images in grayscale. Basal to apical LGE slices are shown from upper left to lower right. Purple contours denote the warped cine myocardium masks generated using the U-net after algorithm step 2 and step 3. Dashed green contours represent manual segmentations of LGE myocardium

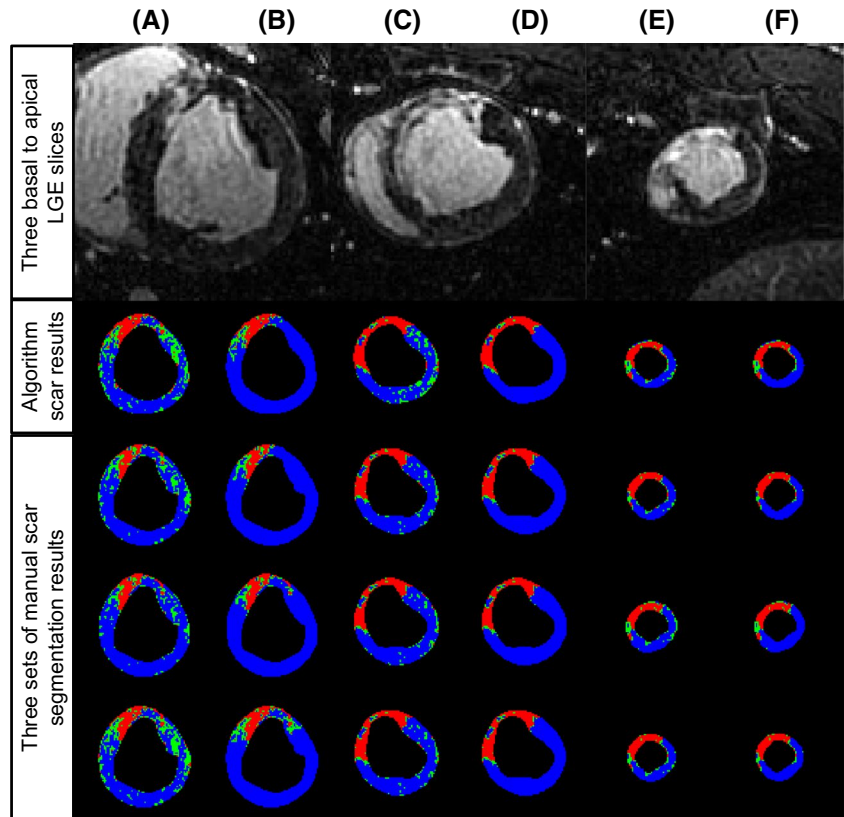
Steps	Region	DSC ([0,1])	ASSD Epic. (mm)	ASSD Endo. (mm)
Cine segmentation	Entire myo.	0.879 ± 0.097	0.91 ± 0.51	0.93 ± 0.56
	Scar region	0.865 ± 0.119	0.94 ± 0.74	1.03 ± 0.82
Cine-LGE registration	Entire myo.	0.913 ± 0.050	0.71 ± 0.33	0.79 ± 0.41
	Scar region	0.901 ± 0.064	0.72 ± 0.39	0.86 ± 0.53
Automated LGE MRI Analysis	Entire myo.	0.859 ± 0.105	1.04 ± 0.54	1.09 ± 0.55
	Scar region	0.832 ± 0.124	1.16 ± 0.82	1.28 ± 0.78

Cine segmentation accuracies were determined by comparing U-net and manual myocardium segmentations. Cine-LGE registration accuracies were evaluated by comparing the warped cine manual myocardium masks and LGE manual myocardium segmentations to only evaluate the effects of the registration methods. For automated LGE MI heterogeneity throughout the study, cine myocardium U-net segmentation was used.

ASSD endo., average symmetric surface-distance for the endocardial contours; ASSD epic, average symmetric surface-distance for the epicardial contours; DSC, dice similarity coefficient; entire myo., entire myocardium; LGE, late gadolinium enhancement.

TABLE 1 Cine myocardium segmentation and cine-LGE registration accuracies (mean \pm SD) for $n = 87$ slices from 10 pigs

FIGURE 3 LGE MI heterogeneity quantification results provided by automated and manual segmentation using the SD method. A) Initial and B) final IC and GZ maps for an LGE slice at the base. C) Initial and D) final IC and GZ maps for an LGE slice at the mid-cavity. E) Initial and F) final IC and GZ maps for an LGE slice at the apex. The first row represents 3 basal-to-apical LGE slices; the second row shows automated algorithm segmentation; and the third to fifth rows correspond to 3 sets of manual results generated by 2 observers. Red: IC; green: GZ; blue: healthy myocardium. IC, infarct core; GZ, gray zone



the 3 LGE images, the initial manual and automated segmentations were “noisy,” and there were substantial false positives in the myocardium that were likely healthy. However, these issues were greatly improved using the normalized cut post-processing (step 3c in Methods) that takes into consideration the relationships of the coordinates of the IC and GZ pixels. To provide an example, the initial automated IC and GZ regions (the second row in Figure 3C) are scattered across the myocardium; the IC and GZ pixels opposite to and far from the scar volume in the LGE (row 1 in Figure 3C-D) are very likely false positives, which need to be corrected. Based on this observation, we designed image features combining IC/GZ pixel location information to filter the scattered false positives and assign these pixels to healthy myocardium. Similarly, the automated and manual MI heterogeneity analysis results of the 3 LGE slices using the FWHM method were problematic, and, as shown in Figure 4, the initial results were much improved using the normalized cut postprocessing (step 3c in Methods). These results suggest that the normalized cut postprocessing component is effective in improving both manual and automated myocardial scar characterization.

Figure 5 shows the relationships and agreements for automated versus manual and F.G. versus T.E.'s manual IC, GZ, and IC + GZ volumes using the SD-based scar quantitation method. As shown in Figure 5 and Table 2, automated IC, GZ, and IC + GZ volumes were strongly and significantly (all Pearson $r > 0.85$, $P < .0001$) correlated with the mean of the 12 sets of manual segmentation generated by 2

observers. The corresponding correlations (r) between automated and manual scar analysis results were similar and not significantly different (Fisher r -to- z transforms $P = .13$ for IC, 0.08 for GZ, and 0.13 for IC + GZ) from interobserver correlations. As shown in Figure 5, the automated algorithm yielded systematically greater IC, GZ, and IC + GZ volumes with biases of 0.03 mL, 0.04 mL, and 0.07 mL, respectively. Comparisons of the mean of the 6 sets of manual measurements generated by F.G. and T.E. showed systematic biases of 0.05 mL, 0.01 mL, and 0.06 mL for IC, GZ, and IC + GZ, respectively.

Figure 6 similarly shows the correlations and agreements between automated versus manual and F.G. versus T.E.'s manual MI heterogeneity measurements using the FWHM method. Figure 6 and Table 2 show that the IC volumes provided by the 2 observers were strongly and significantly correlated (Pearson $r = 0.99$, $P < .0001$), and the correlation was significantly different (Fisher z -score = 0.00) from the correlation of the automated and manual IC volumes (Pearson $r = 0.85$, $P < .0001$). The Bland-Altman bias of the IC volumes for the 2 observers (bias = 0.00 mL) was lower than that between the automated vs manual measurements by the 2 observers (bias = -0.02 mL). For GZ and IC + GZ, the correlations of automated and manual volumes were not significantly different from interobserver correlations (Fisher z -scores = 0.50 for GZ and 0.23 for IC + GZ) and the Bland-Altman biases (0.03 mL for GZ, 0.01 mL for IC + GZ) were lower than F.G. versus T.E.'s manual outcomes (0.11 mL for GZ and 0.11 mL for IC + GZ).

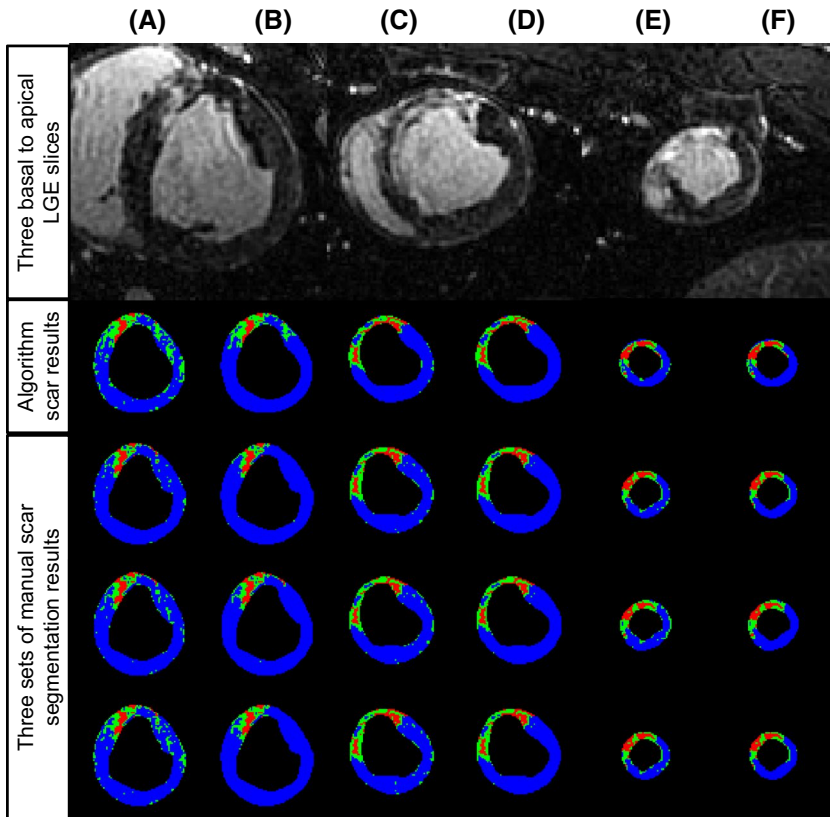


FIGURE 4 LGE MI heterogeneity quantification results provided by automated and manual segmentation using the FWHM method. A) Initial and B) final IC and GZ maps for an LGE slice at the base. C) Initial and D) final IC and GZ maps for an LGE slice at the midcavity. E) Initial and F) final IC and GZ maps for an LGE slice at the apex. The first row represents 3 basal-to-apical LGE slices; the second row shows automated algorithm segmentation; the third to fifth rows correspond to 3 sets of manual results generated by 2 observers. Red: IC; green: GZ; blue: healthy myocardium

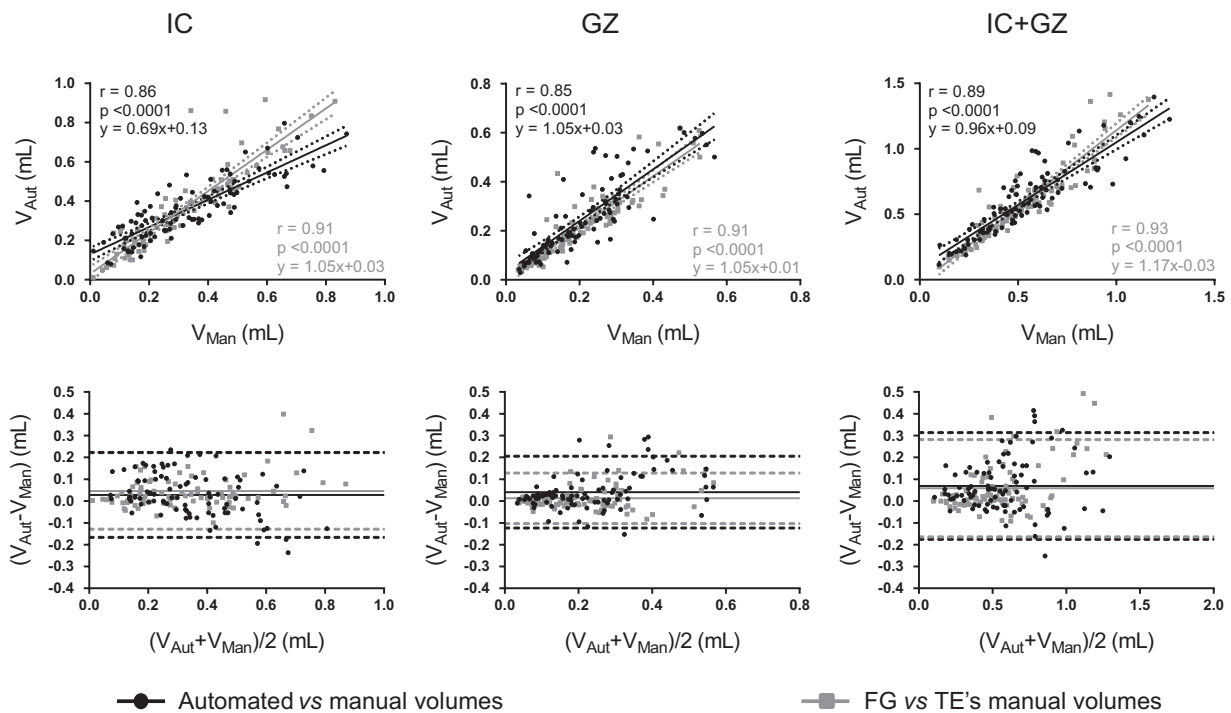


FIGURE 5 Relationships and agreement of automated (V_{Aut}) and manual (V_{Man}) as well as F.G. and T.E.'s manual IC, GZ, and IC + GZ volumes ($n = 87$ slices) using the SD method. Top row: Linear regression of automated and the mean of the 12 sets (6 sets for each manual observer) of manual IC, GZ, and IC + GZ volumes (black), and the mean of the 6 sets of manual results for F.G. and T.E. (gray). Bottom row: Bland-Altman plots of agreement for automated and manually generated (mean of the 12 sets of results for 2 manual observers) IC, GZ, and IC + GZ volumes (black), and the mean of the manual measurements provided by F.G. and T.E. (gray). Solid line indicates the biases, and dotted lines represent the 95% limits of agreement. V_{Aut} , automated volume; V_{Man} , manual volume

TABLE 2 Pearson correlations (r) for Aut. vs. Man. and F.G vs T.E.'s manual IC, GZ, and IC + GZ volumes for $n = 87$ slices from 10 pigs. Fisher z -transformation was used to compare the correlation coefficients

Correlations (r)	SD Method			FWHM Method		
	Aut. vs. Man.	F.G. vs. T.E.'s Man.	Fisher z	Aut. vs. Man.	F. G. vs. T.E.'s Man.	Fisher z
IC	0.86	0.91	0.13	0.85	0.99	0.00
GZ	0.85	0.91	0.08	0.70	0.75	0.50
IC + GZ	0.89	0.93	0.13	0.75	0.82	0.23

Aut.: automated algorithm segmentation; GZ, gray zone; IC, infarct core; Man.: manual segmentation.

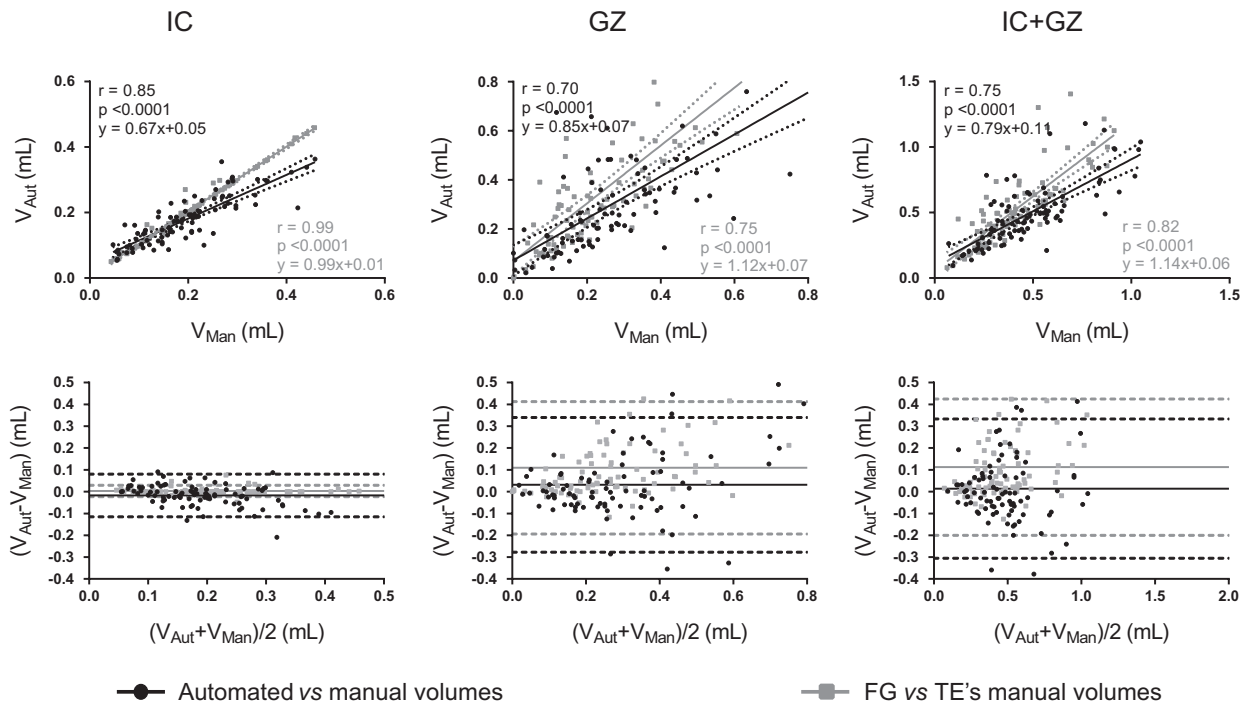


FIGURE 6 Relationships and agreement of automated (V_{Aut}) and manual (V_{Man}) as well as F.G. and T.E.'s manual IC, GZ, and IC + GZ volumes ($n = 87$ slices) using the FWHM method. Top row: Linear regression of automated and the mean of the 12 sets (6 sets for each manual observer) of manual IC, GZ, and IC + GZ volumes (black), and the mean of the 6 sets of manual results for F.G. and T.E.(gray). Bottom row: Bland-Altman plots of agreement for automated and manually generated (mean of the 12 sets of results for 2 manual observers) IC, GZ, and IC + GZ volumes (black), and the mean of the manual measurements provided by F.G. and T.E. (gray). Solid line indicates the biases, and dotted lines represent the 95% limits of agreement

The agreement between automated and manual segmentation as well as interobserver repeated manual segmentation is shown in Table 3. For the SD-based method, the agreement of automated and manual segmentation ($ICC \approx 0.94-0.96$) was similar and comparable to repeated manual quantification provided by 2 observers ($ICC \approx 0.95$). For the FWHM-based method, ICC for automated and manual volumes was lower for IC ($ICC = 0.96$ vs. 0.995) and higher for GZ ($ICC = 0.85$ vs. 0.81) and IC + GZ ($ICC = 0.89$ vs. 0.88) compared with the interobserver agreement. Supporting Information Figure S2 compares the volumes of IC, GZ, and IC + GZ generated by the automated algorithm and multi-observer manual segmentation. For $n = 87$, LGE slices from 10 pigs, the differences between automated and manual scar

TABLE 3 Reproducibility of automated and manual MI heterogeneity quantification

ICC ([0,1])	SD method		FWHM method	
	Aut. vs. Man.	F.G. vs. T.E.'s Man.	Aut. vs. Man.	F.G. vs. T.E.'s Man.
IC	0.943	0.946	0.960	0.995
GZ	0.938	0.945	0.848	0.811
IC + GZ	0.958	0.952	0.892	0.876

Aut.: Automated algorithm segmentation, ICC, intraclass correlation coefficient; Man.: manual segmentation.

Man. vs Man.: Manual MI heterogeneity quantification generated by F.G. and T.E.

TABLE 4 Comparison of the absolute differences (mean \pm SD) between automated vs. manual ($\text{Diff}_{\text{Aut-Man}}$) and F.G. versus T.E.'s manual ($\text{Diff}_{\text{Man-Man}}$) IC, GZ, and IC + GZ volumes (mL) for $n = 87$ slices from 10 pigs.

Differences (mL)	SD method			FWHM method		
	$\text{Diff}_{\text{Aut-Man}}$	$\text{Diff}_{\text{Man-Man}}$	<i>P</i> Value	$\text{Diff}_{\text{Aut-Man}}$	$\text{Diff}_{\text{Man-Man}}$	<i>P</i> Value
IC	0.07 \pm 0.06	0.06 \pm 0.08	.43	0.04 \pm 0.04	0.01 \pm 0.01	< .0001
GZ	0.06 \pm 0.07	0.04 \pm 0.05	.004	0.11 \pm 0.12	0.12 \pm 0.15	.97
IC + GZ	0.10 \pm 0.10	0.08 \pm 0.10	.30	0.11 \pm 0.12	0.12 \pm 0.15	.38

$\text{Diff}_{\text{Aut-Man}}$, absolute differences of automated versus manual; $\text{Diff}_{\text{Man-Man}}$, absolute differences of F.G. versus T.E.'s manual.

volumes (Supporting Information Figure S2A) were similar and within the range of interobserver repeated manual segmentations (Supporting Information Figure S2B). As shown in Table 4, the differences between automated versus manual segmentation volumes were not significantly different ($P > .05$) from the differences between the 2 manual observers except for GZ using the SD-based method ($P = .004$) and IC using the FWHM method ($P < .0001$).

Our approach required approximately 4 h for U-net training, 5 s for generating 50 myocardium segmentation samples in interpolated cine; 1.5 min and 1.0 min for cine-LGE affine and deformable registration, respectively; and 0.2 s per slice for LGE MI heterogeneity quantification, resulting in total runtime of ~ 5 min per dataset.

4 | DISCUSSION

Cardiac MRI-based measurements of MI heterogeneity provide a way to stratify the risk for cardiac arrhythmias, identify candidates for appropriate ICD therapies, and advance efficacious cardiac interventions. In this proof-of-concept study, we developed and evaluated a fully automated approach for cine and 3D LGE registration and MI heterogeneity quantification. We explored a preclinical dataset of 10 pigs with prior myocardial infarction and made some important observations, including: 1) excellent cine myocardium segmentation and cine-LGE registration accuracies for both the entire myocardium and the infarct area; 2) promising IC and GZ volume measurement performance on par with interobserver manual analysis; and, 3) computational efficiency consistent with efficient research and clinical workflows.

First, we achieved excellent cine myocardium segmentation and cine-LGE registration accuracy. LGE provides visualization of heart tissue viability, and quantification of MI heterogeneity requires identification of myocardial contours. However, direct segmentation of the myocardium in LGE is challenging because the contrast between the myocardium and surrounding tissues (eg, blood) is dependent on the selection of inversion time, physiological conditions, noise, and coil factors during image acquisition.³⁶ Recent studies using deep-learning techniques proposed to directly quantify MI heterogeneity in LGE through regression without

myocardium segmentation¹⁷; other studies synthesized LGE-like images³⁷ from noncontrast enhanced anatomical cardiac MRI with reduced demands for LGE myocardium contouring. Although promising, these methods required large datasets and intensive efforts for image annotation for algorithm training (regression methods require dense annotations to generate sparse quantitative measurements), and concerns about algorithm transparency and interpretability remain. To address this issue, we proposed to incorporate the excellent anatomical structural information provided by cine images and to register cine to LGE. For cine segmentation, we employed a standard U-net that has been widely used for various medical image segmentation tasks without introducing extra ambiguity in our algorithm. The segmentation DSC of 0.879 and ASSD of 0.91 to 0.93 mm for the entire cine myocardium are comparable to manual segmentation performance in the literature.^{38,39} In the scar region, the slightly lower DSC of 0.865 and greater ASSD of 0.94 to 1.03 mm are likely a result of the thinned myocardial wall and reduced myocardial volume due to scarring, which increase the difficulty for both automated and manual segmentation. Similarly, we achieved cine-LGE registration DSC of 0.913 and ASSD of 0.71 to 0.79 mm for the entire myocardium with slightly lower DSC of 0.901 and ASSD of 0.72–0.86 mm around the scar region. The DSC and ASSD metrics suggest excellent alignment of the 2 images. We used cine at approximately the end-diastole ± 2 phases and noticed that the selection of cine phase did not affect the cine-LGE registrations too much because of the demonstrated robustness of the affine and deformable registration methods. We note that our approach is highly dependent on cine-LGE registration accuracy, which would benefit from the use of MR images with improved contrast between myocardial infarct and the surrounding tissues. For example, multicontrast late enhancement provides better differentiation of myocardial infarct from healthy myocardium and blood through acquisition of a series of gadolinium-enhancement images at multiple inversion times, generating images with varying contrasts.⁴⁰ Double or triple inversion recovery imaging also provides a way to improve the contrast between myocardium and blood by suppressing the signals from flowing blood, resulting in black-blood images of the heart.⁴¹ Other techniques include magnetization transfer and phase-sensitive inversion recovery.⁴² To our knowledge, this

study provided the first investigation of cine myocardium segmentation and cine-LGE registration performance evaluation around the local scar region in addition to the entire myocardium. The developed cine segmentation and cine-LGE MRI registration components constitute important steps toward integrating high-resolution prior cine and LGE scar maps for applications, including image-guided interventions and computational modeling of electro-mechanical function, which benefit the most from integrated cardiac anatomy and MI heterogeneity information.^{43,44}

Our algorithm provided LGE-derived IC, GZ, and IC + GZ biomarker measurements that were strongly and significantly correlated with manual results. Although manual scar quantification can be performed effectively, this approach requires experienced observers and significant investment of time and expertise, introduces user variability, and is not compatible with an efficient clinical workflow. Notably, the correlations of automated and manual scar volumes were not significantly different from interobserver correlations, that is, Fisher z -scores > 0.05 for comparison of all Pearson correlations (Table 2). In addition, the ICCs between automated and manual scar volumes were similar and comparable to that between the 2 manual observers (Table 3). For the FWHM method, the relatively high ICC of 0.995 for the IC volumes between the 2 manual observers was due to the elimination of manual selection of a hyper-enhanced region and the excellent agreement between repeated manual myocardium segmentation in LGE. As shown in Table 4, for the majority of the experiments automated scar segmentation errors were not significantly different ($P > .05$) from intraobserver repeated manual segmentation except for IC measurements using the FWHM method ($P < .0001$) and GZ using the SD-based method ($P = .004$). We note that LGE MI heterogeneity quantification is a challenging task, and we observed substantial differences between automated versus manual and F.G. versus T.E.'s manual scar volumes in some cases. As shown in Figure 5, our approach tends to underestimate IC volumes for larger IC; this may be because of the use of a relatively large automated remote region, likely resulting in greater SDs and higher thresholds of IC for the SD-based method. Similarly, the use of larger automated remote regions may result in greater maximal image signal intensities and thresholds of GZ/IC + GZ, and therefore, smaller GZ/IC + GZ volumes for the FWHM method. To explore this, we implemented the automated SD and FWHM methods using smaller automated remote regions. In particular, we eroded the largest connected component of the initial automated remote region in step 3b to a maximum size of 100 pixels (similar to the size of manual remote regions), and then used the largest remaining connected component as the final remote regions for automated LGE MI heterogeneity analysis. For the original automated SD method, IC volumes = 0.36 ± 0.16 mL; $r = 0.86$, $y = 0.69x + 0.13$; bias = 0.03 ± 0.10 mL. For the new automated

SD method using smaller remote regions, IC volumes = 0.54 ± 0.26 mL; $r = 0.82$, $y = 0.91x + 0.14$; bias = 0.12 ± 0.12 mL, as shown in Supporting Information Figure S3. Similarly, we implemented the automated FWHM method using the smaller automated remote regions that were used in the new automated SD method. For the original automated FWHM method, GZ volumes = 0.31 ± 0.22 mL; $r = 0.70$, $y = 0.85x + 0.07$; bias = 0.03 ± 0.16 mL. For the new automated FWHM method using smaller remote regions, GZ volumes = 0.38 ± 0.27 mL; $r = 0.79$, $y = 1.13x + 0.06$; bias = 0.10 ± 0.16 mL, as shown in Supporting Information Figure S4. For both experiments, we observed improvements in the IC/GZ volume underestimation (Supporting Information Figure S3 vs. Figure 5, Supporting Information Figure S4 vs. Figure 6), suggesting that the previous IC/GZ volume underestimation in the automated SD/FWHM methods was because of the use of relatively large automated remote regions. The resulting new correlations (r), reproducibility (ICC), and absolute difference ($\text{Diff}_{\text{Aut-Man}}$) between automated and manual IC, GZ, and IC + GZ volumes are provided in Supporting Information Tables S1, S2, and S3, respectively. Overall, the new correlations, agreement, and reproducibility are worse than the original results without erosion.

The differences between automated and manual IC volumes may be attributed to cine myocardium segmentation and cine-LGE registration errors whereby small errors could result in inclusion of tissues with high signal intensities beyond the myocardium (see the bright pixels on the epicardium in the LGE in Figure 3A-B for an example). These observations suggest that the automated remote region selection method requires further investigation, and this represents our future work. Nonetheless, the automated IC, GZ, and IC + GZ volume errors were similar to and within the range of interobserver measurements, as shown in Supporting Information Figure S2 and the paired t tests in Table 4. These results suggest that the MI heterogeneity provided by our approach demonstrates potential worthy of further clinical investigation for assessment of the risk of cardiac arrhythmia and selection of candidates for appropriate ICD therapies. The automated and manual MI heterogeneity results derived using the SD method were different from the FWHM method (Figure 3 vs. Figure 4), and similar results were shown in previous studies.¹⁹ The differences in IC volumes provided by the (automated and manual) FWHM and SD methods are likely because the FWHM method requires identification of a region with high signals (threshold of IC = $0.5 \times$ maximal signal in the myocardium), which is relatively easier and more reproducible than manual selection of a remote region with medium-to-low and homogeneous image signal intensities as for the SD method (threshold of IC = mean + $5 \times$ SD of the signals in the manual remote region). This results in lower variability and potentially higher agreement in IC segmentation for FWHM

compared with the SD method. For GZ segmentation, both FWHM and SD methods require manual selection of a remote region with medium-to-low and homogeneous image signal intensities. In particular, the maximal signal intensity of a single pixel in the remote region is used as the threshold of GZ for the FWHM method; the mean + 2*SD of the signal intensities of a cluster of pixels in the remote region is used as the threshold of GZ for the SD method. Therefore, the threshold of GZ for the FWHM method is likely more variable and dependent on the remote region, whereas the mean and SD of the signals in the remote region, which are used to generate the threshold of GZ for the SD method, are more robust and less variable. This leads to more reproducible and potentially higher agreement in GZ segmentation for SD compared with the FWHM method. Based on this observation, it might be possible to develop a hybrid method that uses FWHM for IC segmentation and SD for GZ segmentation. However, this may result in nonunique classification of myocardial pixels because the threshold of IC may be lower than the threshold of GZ in the hybrid method. We note that clinical applications are more complex and challenging and involve various datasets. Therefore, determination of the validity of this new approach necessitates further and comprehensive evaluation. Regardless, the focus of the current work is to segment and register cardiac MR images with multiple contrasts and to automate the existing scar quantification pipeline as opposed to a comparison of the well-studied SD and FWHM scar quantification methods or development of new LGE analysis methods. In recognition that there is no consensus on the best method for scar quantification, and that both SD and FWHM methods are widely used and clinically accepted, our approach provides a way to automate and expedite the integration of cardiac MR cine images into an existing scar quantification pipeline.

The proposed approach provided rapid and automated cine segmentation, cine-LGE registration, and MI heterogeneity quantification, and was computationally efficient, making it suitable for clinical use. Current implementations of the SD and FWHM methods require substantial user interactions at several points for myocardium segmentation, reference remote myocardium selection, and manual corrections. These steps result in lengthy processing times. The proposed automated approach required less than 5 minutes to register cine and LGE and to generate LGE scar volume measurements and heterogeneity maps for each dataset with accuracy comparable to manual methods. The computational efficiency of our automated algorithm pipeline may be further optimized, for example, using more advanced CPUs and GPUs. As shown in Figures 3 and 4, the initial scar maps generated using the automated and manual methods are “noisy.” The developed normalized cut approach provided a way to effectively “denoise” the initial scar maps without requiring

manual interactions, and the MI heterogeneity quantification required ~0.2 s per LGE slice. Whereas the potential of our approach was demonstrated on $n = 87$ LGE slices containing scar, we also evaluated another 10 slices not containing scar. We observed false positive IC/GZ pixels in these slices for both automated and manual FWHM and SD methods that were implemented in 2D. However, the thresholds of IC and GZ for both automated and manual methods in these slices were substantially lower than in those containing scar. This observation may be used to identify slices not containing scar in future work. In addition, the false positive pixels in LGE slices not containing scar are mainly caused by random noise without a fixed pattern. For example, the “IC/GZ” pixels in these slices are scattered and randomly distributed in the entire myocardium, whereas the IC/GZ pixels in a slice containing scar are patchy and spatially compact. Furthermore, the proposed normalized cut filter in our algorithm takes into account the IC/GZ pixel location information and generates spatially contiguous IC/GZ maps across slices for 3D-based LGE analysis, which could mitigate the false positives (see Figures 3 and 4 for examples). Moreover, 3D LGE images may be analyzed slab by slab, where several contiguous slices are grouped and segmented together using the same IC and GZ thresholds. This may reduce the need to exclude slices not containing scar and further eliminate the potential for false positives. Our approach was based on manual selection of LGE slices containing scar, which we suggest effectively limited false positives without substantially compromising the workflow efficiency. Moving forward with real-time image guided cardiac ablation, it would be beneficial to fuse cine cardiac anatomy and LGE MI heterogeneity information to maximize procedural efficiency and improve patient outcomes. Accordingly, future work will involve optimization of our approach for this and other applications.

We acknowledge several study limitations. We explored a preclinical pig model with myocardial infarct created by occluding the left anterior descending coronary artery; cine and LGE MR imaging were performed under general anesthesia with mechanically controlled respiration. Given this experiment setup, the image datasets and the obtained results likely represent easier cases, and we acknowledge this as a major limitation of this study. To integrate this tool for clinical applications, it is critical to comprehensively validate the performance of our approach on much more diverse patient data. However, since March in 2020, patient studies have been severely restricted due to limitations imposed to manage the COVID-19 pandemic. As a result, the obtained results possibly represent the best-case scenarios, and we caution the interpretation of the derived cine myocardium segmentation, cine-LGE registration, and LGE MI heterogeneity measurements. We note that real clinical applications may involve more complexity and challenges that need to be addressed. For example, in patient imaging it is usually

difficult to control or reproduce the breath-hold levels during cine and LGE image acquisition. These effects may be further aggravated by patients' physiological and pathological conditions, for example, patient motion or cardiac arrhythmia. In addition, the presence of MR-compatible implantable devices may cause imaging artifacts and degraded image quality. Furthermore, the image navigator efficiency may be compromised, slowing the free-breathing 3D LGE acquisitions and producing suboptimal myocardial signal nulling. Together, these factors may cause slice misalignment in the 2D cine stack and partial volume effects through interpolation, imaging artifacts, noise, and suboptimal contrast between myocardium and surrounding tissues in 3D LGE. Compared with the relatively consistent myocardial infarct in a pig model, patient datasets may have more variable LV scar morphology, size, and location; the diversity in the MI patient population could contribute to degraded performance in quantifying MI. There is also evidence that reactive fibrosis leads to remodeling of noninfarcted myocardium, and diffuse fibrosis may begin to develop in noninfarcted regions to compensate for the dysfunctional infarcted myocardium,⁴⁵ imposing further challenges in identifying a true remote reference region that is detrimental to scar quantification. These factors and issues must be carefully considered and addressed before clinical implementation of this approach. In cases of difficulties seen when applying this approach to patient data, we would further optimize the pipeline accordingly. For cine myocardium segmentation, the trained U-net model in this study may be adapted to new patient datasets through transfer learning by fine-tuning the network on a relatively small number of manually segmented patient images. For cine-LGE image registration, we note that several state-of-the-art registration algorithms, for example, NiftyReg (<http://cmictig.cs.ucl.ac.uk/wiki/index.php/NiftyReg>) and Advanced Normalization Tools (<http://stnava.github.io/ANTs/>) have demonstrated excellent performance and have been widely used for various preclinical and clinical applications. These registration algorithms provide a way to facilitate cine-LGE image registration. The subsequent automated remote region selection procedure may be optimized using advanced pattern recognition techniques to mimic manual selection of homogeneous remote myocardium regions. The initial scar maps may be similarly postprocessed using the normalized cut procedure that takes into account the location information and regularizes the contiguity of scar voxels in 3D space. The demonstrated promise on controlled preclinical datasets and the proposed potential solutions suggest that our approach provides promise toward clinical use, which represents the focus of our next efforts. In the current implementation of our algorithm, we used 2D cine stacks of thick short-axis slices, and the partial volume effects impact image quality and downstream analyses. The image quality and anatomical information may be enhanced using higher resolution 3D cine

acquisitions, and we are in the process of optimizing these volumetric image acquisition methods. In addition, we evaluated the performance of our algorithm with fixed thresholds for the SD and FWHM methods, whereas various threshold definitions have been used in the literature. However, currently there is no consensus on the best method to use in the community, and one of the main aims of this work is to improve the usability and reproducibility of existing scar quantification methods. Addressing these limitations represents our future research directions.

5 | CONCLUSION

In summary, we developed and evaluated an approach that provides automated and rapid cine myocardium segmentation, cine-LGE MRI registration, and LGE myocardial infarct heterogeneity quantification with high accuracy, precision, and computational efficiency in preclinical studies, supporting future clinical studies of LGE myocardial infarct heterogeneity analysis.

ACKNOWLEDGMENT


We acknowledge the use of the facilities of Compute Canada. This work was funded by Canadian Institutes of Health Research (CIHR) MOP: #93531, Ontario Research Fund, and GE Healthcare. F.G. is supported by a Banting postdoctoral fellowship.

CONFLICT OF INTEREST

Graham Wright receives research support from GE Healthcare related to this work

ORCID

Fumin Guo  <https://orcid.org/0000-0001-6220-1455>

Philippa R. P. Krahn  <https://orcid.org/0000-0002-5178-4189>

REFERENCES

1. Rubart M, Zipes DP. Mechanisms of sudden cardiac death. *J Clin Invest*. 2005;115:2305-2315.
2. Srinivasan NT, Schilling RJ. Sudden cardiac death and arrhythmias. *Arrhythm Electrophysiol Rev*. 2018;7:111.
3. Nasir N, Pacifico A, Doyle TK, Earle NR, Hardage ML, Henry PD. Spontaneous ventricular tachycardia treated by antitachycardia pacing. *Am J Cardiol*. 1997;79:820-822.
4. Antiarrhythmics versus Implantable Defibrillators (AVID) Investigators. A comparison of antiarrhythmic-drug therapy with implantable defibrillators in patients resuscitated from near-fatal ventricular arrhythmias. *N Engl J Med*. 1997;337:1576-1584.
5. Russo AM, Stainback RF, Bailey SR, et al. ACCF/HRS/AHA/ASE/HFSA/SCAI/SCCT/SCMR 2013 appropriate use criteria for implantable cardioverter-defibrillators and cardiac resynchronization therapy: A report of the American college of cardiology

- foundation appropriate use criteria task force, heart rhythm society, American heart association, American society of echocardiography, heart failure society of America, society for cardiovascular angiography and interventions, society of cardiovascular computed tomography, and society for cardiovascular magnetic resonance. *J Am Coll Cardiol*. 2013;61:1318-1368.
6. Stecker EC, Vickers C, Waltz J, et al. Population-based analysis of sudden cardiac death with and without left ventricular systolic dysfunction: Two-year findings from the Oregon sudden unexpected death study. *J Am Coll Cardiol*. 2006;47:1161-1166.
 7. Bardy GH, Lee KL, Mark DB, et al. Amiodarone or an implantable cardioverter-defibrillator for congestive heart failure. *N Engl J Med*. 2005;352:225-237.
 8. Ursell PC, Gardner PI, Alcala A, Fenoglio JJ Jr, Wit AL. Structural and electrophysiological changes in the epicardial border zone of canine myocardial infarcts during infarct healing. *Circ Res*. 1985;56:436-451.
 9. De Bakker J, Van Capelle FJ, Janse MJ, et al. Slow conduction in the infarcted human heart "zigzag" course of activation. *Circulation*. 1993;88:915-926.
 10. Fernández-Armenta J, Berruzo A, Andreu D, et al. Three-dimensional architecture of scar and conducting channels based on high resolution ce-CMR: Insights for ventricular tachycardia ablation. *Circ Arrhythm Electrophysiol*. 2013;6:528-537.
 11. Kim RJ, Albert TS, Wible JH, et al. Performance of delayed-enhancement magnetic resonance imaging with gadoversetamide contrast for the detection and assessment of myocardial infarction: An international, multicenter, double-blinded, randomized trial. *Circulation*. 2008;117:629-637.
 12. Schmidt A, Azevedo CF, Cheng A, et al. Infarct tissue heterogeneity by magnetic resonance imaging identifies enhanced cardiac arrhythmia susceptibility in patients with left ventricular dysfunction. *Circulation*. 2007;115:2006-2014.
 13. Oduneye SO, Pop M, Shurrab M, et al. Distribution of abnormal potentials in chronic myocardial infarction using a real time magnetic resonance guided electrophysiology system. *J Cardiovasc Magn Reson*. 2015;17:27.
 14. Roes SD, Borleffs CJ, van der Geest RJ, et al. Infarct tissue heterogeneity assessed with contrast-enhanced MRI predicts spontaneous ventricular arrhythmia in patients with ischemic cardiomyopathy and implantable cardioverter-defibrillator. *Circ Cardiovasc Imaging*. 2009;2:183-190.
 15. Yan A, Shayne AJ, Brown KA, et al. Characterization of the peri-infarct zone by contrast-enhanced cardiac MRI is a powerful predictor of post-myocardial infarction mortality. *Circulation*. 2006;114:32-39.
 16. Wu KC, Gerstenblith G, Guallar E, et al. Combined cardiac magnetic resonance imaging and C-reactive protein levels identify a cohort at low risk for defibrillator firings and death. *Circ Cardiovasc Imaging*. 2012;5:178-186.
 17. Zabihollahy F, Rajchl M, White JA, Ukwatta E. Fully automated segmentation of left ventricular scar from 3D late gadolinium enhancement magnetic resonance imaging using a cascaded multi-planar U-net (CMPU-Net). *Med Phys*. 2020;47:1645-1655.
 18. Karim R, Bhagirath P, Claus P, et al. Evaluation of state-of-the-art segmentation algorithms for left ventricle infarct from late gadolinium enhancement MR images. *Med Image Anal*. 2016;30:95-107.
 19. Flett AS, Hasleton J, Cook C, et al. Evaluation of techniques for the quantification of myocardial scar of differing etiology using cardiac magnetic resonance. *JACC Cardiovasc Imaging*. 2011;4:150-156.
 20. Kwon DH, Asamoto L, Popovic ZB, et al. Infarct characterization and quantification by delayed enhancement cardiac magnetic resonance imaging is a powerful independent and incremental predictor of mortality in patients with advanced ischemic cardiomyopathy. *Circ Cardiovasc Imaging*. 2014;7:796-804.
 21. Andreu D, Ortiz-Perez JT, Fernandez-Armenta J, et al. 3D delayed-enhanced magnetic resonance sequences improve conducting channel delineation prior to ventricular tachycardia ablation. *EP Europace*. 2015;17:938-945.
 22. Pop M, Ramanan V, Yang F, et al. High-resolution 3-D T1*-mapping and quantitative image analysis of GRAY ZONE in chronic fibrosis. *IEEE Trans Biomed Eng*. 2014;61:2930-2938.
 23. von Knobelsdorff-Brenkenhoff F, Pilz G, Schulz-Menger J. Representation of cardiovascular magnetic resonance in the AHA/ACC guidelines. *J Cardiovasc Magn Reson*. 2017;19:70.
 24. Ghugre NR, Pop M, Barry J, Connelly KA, Wright GA. Quantitative magnetic resonance imaging can distinguish remodeling mechanisms after acute myocardial infarction based on the severity of ischemic insult. *Magn Reson Med*. 2013;70:1095-1105.
 25. Pop M, Ghugre NR, Ramanan V, et al. Quantification of fibrosis in infarcted swine hearts by ex vivo late gadolinium-enhancement and diffusion-weighted MRI methods. *Phys Med Biol*. 2013;58:5009.
 26. Ronneberger O, Fischer P, Brox T. U-net: Convolutional networks for biomedical image segmentation. 2015. arXiv:1505.04597 [cs.CV].
 27. Warfield SK, Zou KH, Wells WM. Simultaneous truth and performance level estimation (STAPLE): An algorithm for the validation of image segmentation. *IEEE Trans Med Imaging*. 2004;23:903.
 28. Ourselin S, Roche A, Subsol G, Pennec X, Ayache N. Reconstructing a 3D structure from serial histological sections. *Image Vis Comput*. 2001;19:25-31.
 29. Rueckert D, Sonoda LI, Hayes C, Hill DL, Leach MO, Hawkes DJ. Nonrigid registration using free-form deformations: Application to breast MR images. *IEEE Trans Med Imaging*. 1999;18:712-721.
 30. Shi J, Malik J. Normalized cuts and image segmentation. *IEEE Trans Pattern Anal Mach Intell*. 2000;22:888-905.
 31. Guo F, Ng M, Wright G. Cardiac cine MRI left ventricle segmentation combining deep learning and graphical models. In Proceedings International Society for Optics and Photonics (SPIE) 11313, Medical Imaging 2020: Image Processing. Houston, TX, 2020.
 32. Guo F, Ng M, Goubran M, et al. Improving cardiac MRI convolutional neural network segmentation on small training datasets and dataset shift: A continuous kernel cut approach. *Med Image Anal*. 2020;61:101636.
 33. Guo F, Capaldi DP, McCormack DG, Fenster A, Parraga G. A framework for Fourier-decomposition free-breathing pulmonary 1H MRI ventilation measurements. *Magn Reson Med*. 2019;81:2135-2146.
 34. Guo F, Svenningsen S, Kirby M, et al. Thoracic CT-MRI coregistration for regional pulmonary structure-function measurements of obstructive lung disease. *Med Phys*. 2017;44:1718-1733.
 35. Kirby M, Svenningsen S, Owrangi A, et al. Hyperpolarized ³He and ¹²⁹Xe MR imaging in healthy volunteers and patients with chronic obstructive pulmonary disease. *Radiology*. 2012;265:600-610.
 36. Detsky JS, Paul G, Dick AJ, Wright GA, et al. Reproducible classification of infarct heterogeneity using fuzzy clustering on multi-contrast delayed enhancement magnetic resonance images. *IEEE Trans Med Imaging*. 2009;28:1606-1614.

37. Xu C, Howey J, Ohorodnyk P, Roth M, Zhang H, Li S. Segmentation and quantification of infarction without contrast agents via spatiotemporal generative adversarial learning. *Med Image Anal.* 2020;59:101568.
38. Bai W, Sinclair M, Tarroni G, et al. Automated cardiovascular magnetic resonance image analysis with fully convolutional networks. *J Cardiovasc Magn Reson.* 2018;20:65.
39. Bernard O, Lalande A, Zotti C, et al. Deep learning techniques for automatic MRI cardiac multi-structures segmentation and diagnosis: Is the problem solved? *IEEE Trans Med Imaging.* 2018;37:2514-2525.
40. Detsky J, Stainsby JA, Vijayaraghavan R, et al. Inversion-recovery-prepared SSFP for cardiac-phase-resolved delayed-enhancement MRI. *Magn Reson Med.* 2007;58:365-372.
41. Edelman RR, Chien D, Kim D. Fast selective black blood MR imaging. *Radiology.* 1991;181:655-660.
42. Holtackers RJ, Chiribiri A, Schneider T, Higgins DM, Botnar RM. Dark-blood late gadolinium enhancement without additional magnetization preparation. *J Cardiovasc Magn Reson.* 2017;19:1-10.
43. Soto-Iglesias D, Penela D, Jáuregui B, et al. Cardiac magnetic resonance-guided ventricular tachycardia substrate ablation. *JACC Clin Electrophysiol.* 2020;6:436-447.
44. Ciaccio EJ, Coromilas J, Wit AL, Peters NS, Garan H. Source-sink mismatch causing functional conduction block in re-entrant ventricular tachycardia. *JACC Clin Electrophysiol.* 2018;4:1-16.
45. Talman V, Ruskoaho H. Cardiac fibrosis in myocardial infarction—From repair and remodeling to regeneration. *Cell Tissue Res.* 2016;365:563-581.

SUPPORTING INFORMATION

Additional supporting information may be found online in the Supporting Information section.

FIGURE S1 Illustration of the global and regional quantification of cine myocardium segmentation and cine-LGE registration. A) Global quantification of cine segmentation and cine-LGE registration accuracies using the entire myocardium and the complete epicardial/endocardial contours in purple for each slice. B) A bounding box in dashed yellow indicates the scar region used for regional quantification of cine segmentation and cine-LGE registration accuracies C) and the associated segments of the epicardial/endocardial contours D)

FIGURE S2 Comparison of IC, GZ, and IC+GZ volumes generated by automated and manual segmentation. A) Automated and the mean of the 12 sets of manual scar volumes by two observers using the SD and FWHM methods. B) Mean of six sets of the scar volumes provided by FG and TE using the SD and FWHM methods. Values are means for $n = 87$ slices from 10 pigs and error bars represent standard deviation

FIGURE S3 Relationships and agreement of automated (V_{Aut}) and manual (V_{Man}) as well as manual and manual

IC, GZ, and IC+GZ volumes ($n = 87$ slices) using the SD method using smaller automated remote regions through erosion. Top row: Linear regression of automated and the mean of the 12 sets (six sets for each manual observer) of manual IC, GZ, and IC+GZ volumes (black), and the mean of the six sets of manual results for FG and TE (gray). Bottom row: Bland-Altman plots of agreement for automated and manually generated (mean of the 12 sets of results for two manual observers) IC, GZ, and IC+GZ volumes (black), and the mean of the manual measurements provided by FG and TE (gray). Solid line indicates the biases and dotted lines represent the 95% limits of agreement

FIGURE S4 Relationships and agreement of automated (V_{Aut}) and manual (V_{Man}) as well as manual and manual IC, GZ, and IC+GZ volumes ($n = 87$ slices) using the FWHM method using smaller automated remote regions through erosion. Top row: Linear regression of automated and the mean of the 12 sets (six sets for each manual observer) of manual IC, GZ, and IC+GZ volumes (black), and the mean of the six sets of manual results for FG and TE (gray). Bottom row: Bland-Altman plots of agreement for automated and manually generated (mean of the 12 sets of results for two manual observers) IC, GZ, and IC+GZ volumes (black), and the mean of the manual measurements provided by FG and TE (gray). Solid line indicates the biases and dotted lines represent the 95% limits of agreement

TABLE S1 Pearson correlations (r) for automated vs manual (Aut. vs Man.) and FG vs TE's manual (Man. vs Man.) IC, GZ, and IC+GZ volumes for $n = 87$ slices from 10 pigs. Fisher z-transformation was used to compare the correlation coefficients. Automated SD and FWHM segmentation results were based on smaller automated remote regions through erosion

TABLE S2 Reproducibility of automated and manual MI heterogeneity quantification. Automated SD and FWHM segmentation results were based on smaller automated remote regions through erosion

TABLE S3 Comparison of the absolute differences (mean \pm SD) between automated vs manual ($\text{Diff}_{\text{Aut-Man}}$) and FG vs TE's manual ($\text{Diff}_{\text{Man-Man}}$) IC, GZ, and IC+GZ volumes (mL) for $n = 87$ slices from 10 pigs. Automated SD and FWHM segmentation results were based on smaller automated remote regions through erosion

How to cite this article: Guo F, Krahn PRP, Escartin T, Roifman I, Wright G. Cine and late gadolinium enhancement MRI registration and automated myocardial infarct heterogeneity quantification. *Magn Reson Med.* 2021;85:2842–2855. <https://doi.org/10.1002/mrm.28596>